Optimizing Requirements for a Compact Spaceborne Adaptive Spectral Imaging System in Subpixel Target Detection Applications

Sanghui Han, *Student Member, IEEE*, John Kerekes, *Senior Member, IEEE*, Shawn Higbee, and Lawrence Siegel

***Abstract*—We developed a process to provide design recommendations for compact spaceborne spectral imaging systems with adaptive band selection capabilities. Our focus application was subpixel target detection, and we analyzed a set of mission scenarios to find relationships in detection performance between selected parameters of interest. We used an analytic model to predict performance and generate trade curves, then simulated a scene to analyze potential operational effects on performance for the selected target and background combinations. Using these models, we predicted and assessed each scenario to provide recommendations for mission feasibility and system design. The parameters we selected for analysis were target fill fraction, noise, number of bands, and scene complexity to find critical points in the trade space and reach a set of recommendations. We examined the operational effects by simulating a realistic scenario and ensuring key real-world phenomena were captured within the spectral images. Our results produced recommendations for each mission and provided a proof of concept for a process to analyze designs of miniature spaceborne imaging systems.**

***Index Terms*—Band selection, hyperspectral imagery, imaging system design, modeling, optimization, remote sensing, simulation, target detection.**

I. Introduction

THERE are many design requirements for an Earth observing remote sensing system, and when using miniature spaceborne systems to collect spectral images, there are several considerations that require analysis. With panchromatic imaging systems, the trade space for optimizing the image quality resides mostly in the spatial domain. On the other hand, the spectral component of images often make design optimization more complex. In this article, we analyze the utility of spectral images for subpixel target detection applications focused on compact systems with adaptive band selection capabilities. However, this process can be modified for larger more general systems with different thresholds for the parameters analyzed and further examination of other components that affect utility. What makes this process specific to miniature systems, and more specifically, one that had adaptive spectral capabilities is the hardware that motivated this work.

In this article, we present an end-to-end process for analyzing the design and operations of compact spectral imaging systems with the combined use of an analytic model and physics-based simulation. In Section II, we frame our problem and present our operational process, which served as our constraint. Then, in Section III, we present the figures of merit, detection algorithms, and modeling tools we used for prediction and assessment processes. In Section IV, we explain our approach to exploring the trade space for spectral image utility. We conclude this article with our results in Section V where we provide example design recommendations, and suggestions for future work in Section VI.

Manuscript received September 6, 2019; revised January 13, 2020 and May 9, 2020; accepted May 10, 2020. Date of publication May 12, 2020; date of current version July 17, 2020. This work was supported by the U.S. Department of Energy by Lawrence Livermore National Laboratory under Contract DE-AC52-07NA27344. *(Corresponding author: Sanghui Han.)*

Sanghui Han and John Kerekes are with the Department of Imaging Science, Rochester Institute of Technology, Rochester, NY 14623 USA (e-mail: sxh8907@g.rit.edu).

Shawn Higbee and Lawrence Siegel are with the Department of Defense and Security, Lawrence Livermore National Laboratory, Livermore, CA 94550 USA.

Digital Object Identifier 10.1109/JMASS.2020.2994273

II. Motivation

The process and results we present in this article were applicable to compact spaceborne spectral imaging systems with adaptive band selection capabilities deployed for a wide-area search of subpixel targets. The utility of the imaging system would produce detection performance sufficient to tip and cue other information collection capabilities to confirm or deny the presence of an object. We present an example mission scenario to search for vehicles in a desert and suburban locations. However, the simulation can be modified to replicate other scenarios, such as plume detection or open ocean route safety assessment. A single spectral image collected of these areas, could relay several locations with the potential presence of a target, and an overlap from other sources of intelligence with any of these locations would tip an asset capable of characterizing the target. As a part of the design process, we first determine mission feasibility, then if a target was indeed viable

This work is licensed under a Creative Commons Attribution 4.0 License. For more information, see https://creativecommons.org/licenses/by/4.0/

for a miniature spectral system, we determined the optimal design. The analysis data from the design analysis can be used in the operational process for collection decisions.

We analyzed the mission feasibility and optimal design parameters for a system that was less than 10 kg and 30–60 cm on each side, with a low-Earth orbit, and therefore, the size of the optical diameter was limited [1]. Each unit was self-contained with its own communication, power, and navigation system within the spacecraft, and a single unit would be a part of a constellation of miniature satellites to meet various requirements. The system and operational context we envisioned were a miniature system such as a CubeSat with existing system components that could be modified to produce a small range of focal lengths and an existing sensor that could be replaced to reduce noise, but at a cost. Parameters that encompassed these components that could lead to decisions for them were selected for analysis and the process was refined after several iterations to produce recommendations for use in real operations in deploying the miniature systems for specific missions. The parameters we selected to limit the scope of our analysis were to determine the best configuration of the existing optics for a small range of spatial resolutions and whether or not the cost of reducing the noise of the existing sensors was justified. This analysis was a continuation of our study that analyzed the utility trade space in the spatial domain for a system with fixed optical diameter that changed the noise and the point spread function as the focal length changed [2].

The previous methods for predicting spectral image utility as well as design optimization methods were considered. Some of the past methods we examined that predicted spectral image utility, empirically derived equations similar to the general image-quality equation (GIQE) for panchromatic images [3]. They developed a regression model using real spectral images to produce an equation [4]–[6]. Other approaches combined spatial and spectral figures of merit [7] or used statistical parameters of an image and the target to predict detection performance [8].

The previous methods for optimizing the system design also used simulation and modeling of spectral imaging systems [9] and encompassed the entire remote sensing process [10]. Trade studies were also conducted previously using both analytic and simulation models for spectral imagery to configure complex data selection parameters [11]. Other methods for studying system designs from a mission and operation perspective exist for satellite systems where the optimal design of small satellites is outlined in detail for a list of mission objectives [12]. More recent processes that were developed that facilitated decision making on the design of remote sensing satellites used an approach called multidisciplinary design optimization [13] and multiparameter joint optimization [14]. A study that analyzed the use of modeling for the design of CubeSats considered the multiple dependencies between the design and operation and can be considered the state of the art [15]. These methods for analyzing miniature systems can be used for designing and deploying remote sensing satellites with specific application objectives. What we present in this article is a process to analyze subpixel target detection using spectral images to provide recommendations for mission feasibility, design optimization, and operational decision making.

A recent state-of-the-art system that lends itself to "end-to-end" analysis is the Compact High-Resolution Imaging Spectrometer (CHRIS) of the European Space Agency Third-Part Mission Project for On-Board Autonomy (PROBA). This system is capable of making the trade between spectral resolution and spatial resolution [16], depending on the mission. Whether it is for land use classification [17] which requires more bands, but lower spatial resolution or chlorophyll content analysis [18], which requires less bands but higher spatial resolution, the system is capable of collecting images for each purpose. We developed a process to analyze the compact spectral imaging system trade space with subpixel target detection as the focus application. The underlying assumption for the miniature systems designed using this process was that the data collected will be automatically processed and a part of initiatives to use artificial intelligence in-orbit [19].

The process we propose begins with a few selected mission scenarios, assumes that the bands can be selected as the target changes prior to collection, and works within the constraints of miniature systems. Our assumption was that these compact spectral imaging systems would only be required to detect a few or a single target as part of the constellation of satellites. We build on the previous work that developed frameworks to predict spectral image utility [20] and assess small satellite performance and suitability for wide-area search missions [21]. This article is a continuation of work to analyze adaptive band selection capabilities of the miniature systems where we validated a band selection method using real images [22]. This study also confirmed the congruence of the results from the modeling tools we use in this article and validated their combined use.

III. Background

There were many components that affected subpixel target detection performance, but what drove utility was the target itself and the scene it was in. Materials with low reflectance throughout most of the spectrum were more difficult to detect than materials with high reflectance. The detectability of an object was also affected by the background location and its characteristics. In this section, we describe the figures of merit and the parameters of spectral utility that was the focus of our analysis. The four parameters of the spectral imaging trade space we selected that encompassed the adaptive band selection capabilities of a miniature satellite that had a few components available for limited modification were target abundance, number of bands, noise, and background complexity. The metrics we used facilitated the analysis of subpixel target detection performance that determined feasibility recommendations and system optimization.

A. Utility

When quantifying detection performance, there were two metrics that were often used: true positive rate (TPR) at a specified false-positive rate (FPR) or the area under the curve (AUC). For this project, we used a combination of the two

metrics that defined utility as the AUC below a specified FPR weighting function (ψ) scaled by the perfect detection area possible for the selected FPR based on [8]

$$\text{Utility}_{\psi} = \frac{\int_{i=0}^{1} \psi \cdot \text{TPR}(\mathbf{t}, \text{TA}, D(\mathbf{t}), \text{FPR})\, d\text{FPR}}{\int_{i=0}^{1} \psi\, d\text{FPR}}. \quad (1)$$

In this equation, $\mathbf{t}$ is the target reflectance and $D(\mathbf{t})$ is the detection performance for that target at the selected target abundance or target fill fraction (TA). We used this metric in order to standardize our prediction and assessment results for comparison and for its ability to better characterize the overall performance. We wanted to measure the utility for a range of FPRs without having to repeat our process for multiple FPRs. Using this metric, if the utility value was low, we could expect that performance at lower FPRs was low, and if the utility was high, then performance was likely sustained even for lower FPRs. We selected an FPR of 0.001 for analysis as this was what we determined to be the upper limit of acceptable false alarms in most performance evaluations and operations. For a 300×300 pixel image, FPR $= 0.001$ was equated to 90 pixels per image for our analysis, within areas that were about 2.5 km^2 when the ground sampled distance (GSD) was 5 m, and 20 km^2 when the GSD was 15 m. What was not considered for our work was the utility contributions of the total scene size as GSD increased where a larger scene would be capable of providing more context and allowed larger area coverage with less data processing requirements. These effects on utility are possibly a subject for future study.

B. Spectral Signature Comparisons

A challenging aspect of predicting spectral image utility for subpixel target detection was that the target material, background, and their separability contributed to the detection probability. We used a method for quantifying how similar or different one material was from another by calculating the spectral similarity value (SSV) [23]. The SSV combined the Euclidean distance

$$d_e = \sqrt{\frac{1}{N}\sum_{i=1}^{N}(x_i - y_i)^2} \quad (2)$$

and the correlation coefficient

$$r^2 = \left(\frac{\frac{1}{N-1}\sum_{i=1}^{N}(x_i - \mu_x)(y_i - \mu_y)}{\sigma_x \sigma_y}\right)^2 \quad (3)$$

$$\hat{r}^2 = 1 - r^2 \quad (4)$$

to quantify the separability of the spectral reflectance curves of two materials

$$\text{SSV} = \sqrt{d_e^2 + \hat{r}^2}. \quad (5)$$

The mean spectrum of material reflectance X (μ_x) and the standard deviation (σ_x) of the spectral variations were compared to that of material Y, for the number of bands (N). The more distinct X and Y were, the larger the SSV which had a maximum value of $\sqrt{2}$. This combined the magnitude of the material spectrum (d_e) as well as the shape of the curve ($\hat{r}^2$)

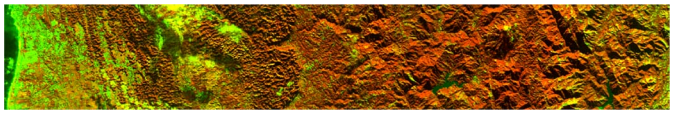

Fig. 1. Hyperion image of the coast of Japan shown with bands 2, 5, and 10—B(365.76 nm), G(396.29 nm), and R(447.17 nm). Example of a scene with high degree of complexity.

Fig. 2. Hyperion image of the coast of Japan shown with bands 2, 5, and 10—B(365.76 nm), G(396.29 nm), and R(447.17 nm). Example of a scene with low-complexity value.

to determine how distinct one material was from another. This value accounted for the spectral reflectance characteristics of materials where the difference in the magnitudes of the curves determined whether or not they were distinct. The correlation coefficient accounted for differences in the measurements of the same material that may have different magnitudes, but retains the same shape, and so a low $\hat{r}^2$ would mean two materials have similar shape in their reflectance spectra, even if the Euclidean distance was high due to differences in measurement conditions.

C. Scene Complexity

The complexity of a scene that affected detection performance was contributed by the number of materials that were present, the variance calculated from multiple measurements of each material's spectrum, and the homogeneity of the scene. A homogeneous scene was one that was relatively uniform, and a heterogeneous scene was one that was composed of different structures. Also the brightness of the background materials affected detection performance. Fig. 1 shows a background that would decrease performance due to its complexity and the brighter materials present. In this scene, there are bright materials and structures that add to the complexity by increasing material measurement variations due to shadows or object geometry, variations due to the number of materials present which makes this a heterogeneous scene. Fig. 2, on the other hand, is an ideal background scene where it is composed mostly of water which is dark with low reflectance throughout the spectrum, with the minimal structure that introduces material measurement variations from 3-D geometry effects such as shadows, and makes this a homogeneous scene.

In order to quantify the degree of scene complexity in our analysis, we used two methods. The first method was used in our prediction and calculated as a part of the analytic model. We combined the mean spectral signatures of the materials that composed the background and their covariance matrices

$$\Gamma = \sum_{i=1}^{K} a_i \sqrt{\mathbf{b}_i^T \cdot \Sigma_i \cdot \mathbf{b}_i}. \quad (6)$$

Here, the number of different materials that the background was composed of was K, and $\mathbf{b}_i$ were the spectral signatures of a single material, and Σ_i was its covariance from the measurement variations in each band. The spectral signature and the covariance were scaled by the fractional amount (a_i) that material was present in the background composition. The background complexity value (Γ) was used in our prediction step to parameterize the background effects. The background composition with the specific materials and their fractions could be modified as part of the prediction model, and so several material spectra were selected for each scene. The material brightness was accounted for in the complexity value in (6) so brighter materials increased the complexity to a greater extent, and darker materials contributed less to the complexity. What this value did not account for was the degree of homogeneity of the scene. This metric was appropriate for the prediction, but for the assessment, we used a method that could account for scene heterogeneity.

We used a geometric approach to quantify scene complexity in our assessment step. When a hyperspectral image was represented geometrically, the *endmembers* of the HSI formed the vertices of the space that the data occupied [24]. This approach estimated the volume of a convex set that would be enclosed by the *endmembers* present in a scene if the number was known [25]. The volume of a scene when the number of endmembers present was not known was calculated by finding the parallelotope using the Gram matrix of the image between each pixel for a range of endmembers $k = 3, 4, 5, \ldots, M$

$$\mathbf{G}_{i,j} = <\mathbf{x}_i, \mathbf{x}_j>. \tag{7}$$

The Gram matrix was the same size as the spatial dimensions of the image. The determinant of the Gram matrix was the square of the volume of the parallelotopes for $k = 3, 4, 5, \ldots, M$ endmembers

$$V_k = \text{norm}_k\left(\sqrt{\det(\mathbf{G})}\right). \tag{8}$$

The volume was calculated for each k and normalized to allow the k-dimensional values to be comparable, and the normalized maximum volume within the selected range determined the scene complexity for the input image

$$V_{\text{scene}} = \max\left(V_k|_{k=3}^{M}\right). \tag{9}$$

For our analysis, M was set to 15, as this estimated the maximum number of materials present in the entire scene. The maximum k value was 12 for the most complex subset scene and $\text{V}_{\text{scene}} = 0.82$, and $k = 5$ for the least complex subset scenes with $\text{V}_{\text{scene}} = 0.30$. M could be selected by the user based on the estimated maximum number of materials present in the scene. This value could be easily changed after examination of a few k versus V_k plots. The subset scenes with larger volumes consisted of many materials that were brighter, and had a high degree of heterogeneity. This method accounted for all three aspects of scene complexity where higher volume was consistent with brighter materials. However, if a scene was uniform even if it was composed of bright materials, it had low volume. While darker materials occupied less volume in general, a heterogeneous scene with high in-scene variation had a higher volume than a uniform scene. Therefore, like the background complexity value (Γ), the scene volume (V_{scene}) accounted for the brightness of the material's spectral signature, measurement variance of individual materials, and their contribution to scene complexity. Unlike Γ however, it also accounted for the degree of uniformity in a scene due to the structures and the variations in their presence within the scene.

D. Target Detection

We selected three target detection algorithms to calculate performance based on their wide use with HSI [24]. We selected spectral angle mapper (SAM) as one of the algorithms, because it calculated the difference in the angle between the target and background to determine the likelihood of a target's presence [26]. This method was an example of an algorithm that used a distance metric. The adaptive cosine estimator (ACE) was another method we used as it was considered state of the art [27]. It also used a distance metric, but accounted for some degree of randomness within the background by incorporating the inverse covariance of the data, which could improve the detection of subpixel targets. The third detection algorithm we used was the spectral matched filter (SMF), which calculated the orthogonal vector space, and subtracted the mean spectrum from the pixel spectra [28]. We selected this method because of its similarity to the constrained energy minimizer (CEM), which also used the orthogonal vector space. The CEM was the algorithm that was implemented in the analytic model that was used to predict utility [29]. Implementing other detection algorithms in the prediction tool was outside of the scope of this project, but can be explored in future work. We compared the three algorithms to ensure that the results of our utility analysis did not hinge on a single detection algorithm's calculation metric. Any target, imaging system, scene, atmospheric compensation error, or other manifestations of spectral imaging system characteristics, could produce different results for each target detection method. By comparing the algorithms, we could detect any anomalies in our utility analysis that stemmed from the detection algorithm itself as opposed to the system design or mission.

E. Simulation and Modeling Tools

We used two modeling tools to analyze the trade space for compact spectral imaging systems. For the prediction process, we used an analytic model that used first- and second-order statistics. Then for the assessment process, we used a physics-based simulation model to generate spectral images that could replicate the operational images of a realistic scene. The combined use of both tools allowed us to forego the labor-intensive process of modifying a simulation and running hundreds of iterations to generate trade curves for the four parameters we analyzed. The prediction tool generated trade curves for each parameter in a matter of minutes to find critical points in the trade space, and the simulation tool was used to validate and refine the results from the prediction process.

1) FASSP: The analytic modeling tool used for the prediction process was forecasting and analysis of spectroradiometric system performance (FASSP), which calculated the subpixel target detection statistics of remotely sensed spectral imaging systems [30]. FASSP was a model that accounted for each component of the imaging chain to predict performance. This model generated receiver operating characteristic (ROC) curves and trade curves using the CEM algorithm. It calculated the final sensor reaching radiance from the composition of target and background input spectra, and accounted for the atmosphere, collection geometry, illumination conditions, and noise.

The user defined the illumination and atmospheric conditions that were modeled using moderate resolution transmission (MODTRAN) [31], target pixel fill fractions (target abundance), target and background spectral reflectance data, background composition with any combination of materials possible, and sensor characteristics. The spectral reflectance signatures of the targets and various background materials were combined to model complexities seen in real scenes. A linear mixture model was used to calculate the final spectral radiance of the material combinations, but variance associated with multiple measurements in each reflectance file could produce results that were consistent with real images. The variance of each material spectra was calculated from hundreds of ground measurements using a spectrometer.

We used the FASSP modeling tool to efficiently generate trade curves and determine the critical points in the trade space for spectral images [32]. It was a tractable method that could account for the primary components of the imaging chain to predict performance and narrow the simulation design. It allowed us to analyze the four components of the compact systems in a few runs that took a matter of minutes on a personal computer. The same process to generate trade curves for these components would have taken hundreds of simulation designs, each a painstaking process that would have been time consuming and cumbersome.

2) DIRSIG: For the assessment process, we used a physics-based image simulation tool to generate spectral images that replicated the operational context of the images collected by the miniature spaceborne systems. Digital imaging and remote sensing image generation (DIRSIG) uses a ray-tracing approach that accounts for the random nature of light scattering and accounts for various phenomena including adjacency effects. Using the DIRSIG model, we designed a scene and replicated the conditions in which the spectral images would be collected to generate images that were used to assess subpixel target detection performance [33]. This model accounted for each imaging chain component similar to FASSP, using MODTRAN to model the atmosphere and illumination conditions, sensor characteristics with collection geometry, and spectral information of the materials in the scene. However, with DIRSIG, we also recreated a real location where we placed 3-D structures and on realistic terrain using design software and attributed each object in the scene with its own material spectra. Therefore, with FASSP, we were able to predict detection performance for a set of background compositions and a range of target fill fractions, but with DIRSIG, we designed a heterogeneous scene with hundreds of structures with their own spectra to generate spectral images. We recreated the operational aspect of image collection by producing a target abundance distribution that was from an object's spatial location relative to the collection geometry, sensor design, and size. The simulation was designed to produce images with a target and other objects in the scene that changed its location at given time increments to generate time-correlated images.

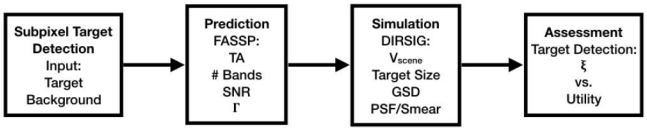

Fig. 3. Diagram of approach to analyze spectral image utility.

IV. Approach

We explored the utility trade space to provide recommendations for mission feasibility and optimal system design by first predicting performance, then assessing simulated images. We tested four target materials against two background types as example cases. We accounted for band selection prior to collection to optimize the trade between adequate performance and reducing data processing requirements. We predicted utility to test TA, number of bands, noise, and background complexity and found critical points in the trade space. Once we determined critical points, we designed a scene to simulate the collection conditions in a realistic scene that encompassed the predicted critical points in the trade space. Fig. 3 shows a diagram of the approach with the variables analyzed in each step.

A. Targets and Backgrounds

We selected two difficult and easy targets that were tested with two background types. The two difficult targets were black and green materials which had relatively low reflectance values in the visible near-infrared (VNIR) portion of the spectrum (0.4–1.0 μm). The two easy targets we selected were white and orange materials. Fig. 4 shows the mean spectral reflectance values of the four targets along with the standard deviations of the individual material measurements that are shown by the gray area.

The two backgrounds we selected were composed of multiple types of sand and grass spectra. The backgrounds were selected not only for their prevalence in target detection but also because of their contrast to the four targets we selected. The green and orange targets had relatively high SSVs compared to the grass background, and so we had one easy and one difficult target that was less spectrally distinct to the grass background. In a similar manner, the sand background was composed of materials that were less spectrally distinct from the white and black targets. Figs. 5 and 6 show the four mean spectral reflectance curves used to compose the two background types along with their standard deviations of the measurements shown by the gray area.

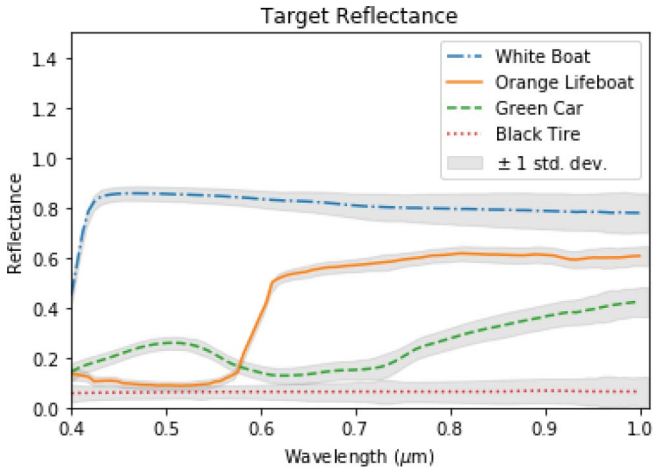

Fig. 4. Target reflectance curves used for FASSP analysis and DIRSIG objects placed in scene. Also used to select bands. Standard deviations calculated from measurement variations shown by the gray area.

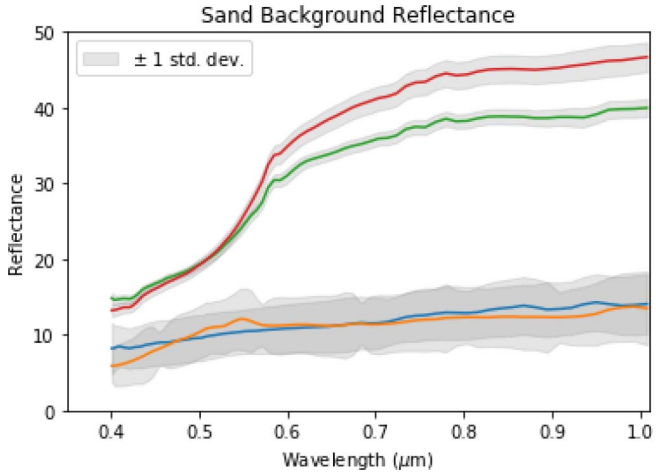

Fig. 6. Background reflectance curves used to compose sand background used for FASSP and DIRSIG scene. Standard deviations calculated from measurement variations shown by gray area.

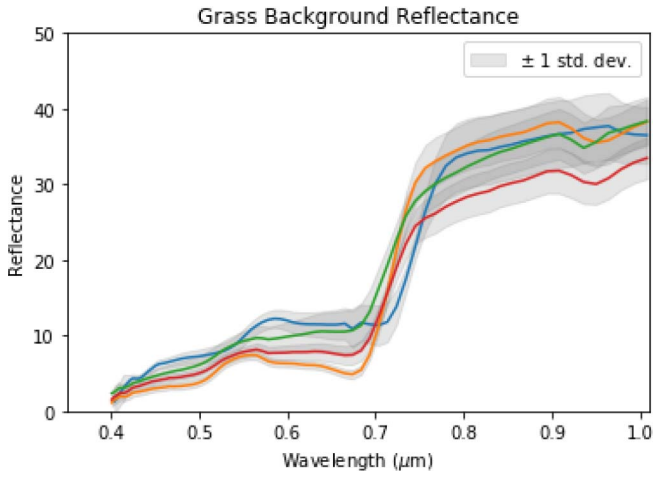

Fig. 5. Background reflectance curves used to compose grass background used for FASSP and DIRSIG scene. Standard deviations calculated from measurement variations shown by the gray area.

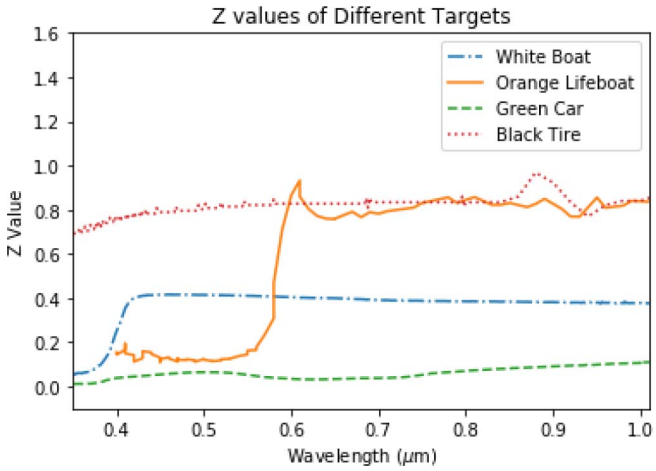

Fig. 7. Normalized **z** values of band selection methods for the bands between 0.4 and 1.0 μm. The highest **z** values are selected.

B. Band Selection

We used a band selection method that used only the target reflectance signature to rank order the best bands [22]. While there were other state-of-the-art methods that could achieve high performance, these methods were inappropriate for a miniature system due to their calculation complexity. For the operational process we envisioned and the capabilities of the system we assumed, i.e., adaptive band selection, we needed a method that was simple and did not need background information. The bands from only the target spectrum (BOTS) method rank-ordered bands using the magnitude and slope of the target spectral reflectance

$$\mathbf{z} = a \cdot \frac{d\mathbf{t}}{d\lambda} + b \cdot \mathbf{t}; \quad a + b = 1. \tag{10}$$

The coefficients of the BOTS method could be modified to allow flexibility for different situations. The combination could be changed based on the type of target or background complexity. In [22], the optimal coefficient was found to be $a = 0.2$ for the easy detection scenario, and $a = 0.8$ for the difficult scenario. The difficulty of a detection scenario is a combination of the target and dominating background spectra and their separability, but with the brightness of the target as the dominating factor. We used $a = 0.2$ for the orange and white targets, and $a = 0.8$ for the black and green targets. These coefficients are user selected and for this study were empirically determined after analysis of the target [34]. The effects of using different coefficients on utility for other targets and scenarios and quantifying the difficulty level of a detection scenario are possible subjects for future study.

Fig. 7 shows the normalized **z** values that were calculated using BOTS with the coefficients based on the target types. The bands that corresponded with the highest 30 **z** values for each target were used for the trade space analysis. The number of bands beyond 30 was not analyzed due to the limitations posed by the computation requirements to calculate the detection probability of more bands. We assumed for the automated image exploitation architecture of the miniature satellite imaging systems, any mission that required greater than 30 bands would not be feasible.

TABLE I
INITIAL COMPOSITION OF THE SAND BACKGROUND

Background Spectrum	Percentage Composition
Ocean Sand	10%
Dirt Road	60%
Light Dirt Road	20%
Gravel	10%
Total	**100%**

TABLE II
INITIAL COMPOSITION OF THE GRASS BACKGROUND

Background Spectrum	Percentage Composition
Grass 1	10%
Grass 2	20%
Vegetation 1	40%
Shrubbery	30%
Total	**100%**

C. Utility Prediction: FASSP

We initialized components of the trade space for noise and Γ to generate the trade curve for TA. The relative calibration error was set to 5%, which resulted in a maximum signal-to-noise ratio (SNR) of 20 but varied for each band. This introduced random error (not systematic) and the SNR that resulted was consistent with the initial expected miniature system detector performance. Initial background complexity values were determined by using the four shown in Tables I and II to compose the background. The initial Γ values for the sand background were $\Gamma = 0.17$ and $\Gamma = 0.075$ for the grass background. TA was analyzed initially for the range of 0.01–0.99 in 0.15 increments. The lowest TA where the Utility_{ψ} reached perfect detection was determined as the critical point for each scenario and we narrowed the analysis to 0.01 increments at these points.

The sensor model we used as part of the prediction was for the hyperspectral digital imagery collection experiment (HYDICE) sensor which collects 210 bands in the range of 0.35–2.5 μm [35]. We used bands 4–97 of this sensor to generate the trade curves for TA. Any reference in this article to use *all* the bands refers to this subset of the HYDICE sensor. While the miniature system was tunable over time and so the spectral bandwidth and center wavelength could be changed as needed, we used the fixed bands of the HYDICE in our analysis to keep our problem tractable as this was a well-characterized sensor. The adaptability of the miniature system was modeled by the bands selected for analysis using BOTS. However, implementing a tunable spectral sensor and analyzing its effects on utility are worthy future endeavors.

Once we found the critical points in the trade curves for TA, we used these points as the input values to analyze the number of bands. We generated trade curves for 2, 5, 10, 15, 20, 25, and 30 bands, and determined the effects of reducing the number of bands. The lowest number of bands with $\text{Utility}_{\psi} > 0.9$ was determined to be the critical point. If a critical point was found, it was used as input for the noise analysis. For scenarios with $\text{Utility}_{\psi} < 0.9$ even when using 30 bands, we analyzed noise with both 30 bands and all the bands as input. We tested the noise effects by setting the calibration errors to result in maximum SNRs of 5, 10, 20, 30, 40, and 50 that varied from band to band from atmospheric effects. This range of SNR values encompassed the initial compact system detector performance and was used to determine whether or not improving system noise performance justified the cost of doing so. However, this did not analyze each fixed and random component of noise which we leave as a potential future study.

The final dimension in the trade space we analyzed was Γ. We calculated the Γ values by changing the composition of the four curves that were used for each background type. Increasing the percentage of spectral reflectance curves that had higher variation or higher reflectance to compose the background increased Γ. Therefore, we traversed through the spectral image utility trade space by analyzing the four parameters of interest and finding the critical points. This produced results that could be used to determine mission feasibility and provide system design recommendations.

TABLE III
PARAMETERS SELECTED FOR THE OPTICAL SYSTEM SIMULATION

Imaging System Parameters		Notes
Aperture Diameter	44.5mm	F/2.4 - F/7.1
Effective Focal Length	105-315mm	5-15m GSD
Spectral Bandwidth	0.4-1.0 μm	94 bands
Spectral Resolution	6.19nm	Narrow response function
Pixel Pitch	4.5 μm	Square detectors
Integration Time	0.6 ms	Produce smear
Sensor Altitude	350 km	
Look Angle	Nadir	
Illumination Angle	Solar Zenith	

D. Assessment: DIRSIG

Using our simulation tool, we generated spectral imagery of scenes that could test the utility predictions. The GSDs we determined that encompassed the critical points were 5, 10, and 15 m and we placed vehicles of varying sizes in our scene that could produce the TA critical points for all the scenarios. Table III shows the imaging system parameters we simulated. These were congruent to the simulation validation study where we developed the techniques to ensure we replicated the real-world parameters that affected image quality metrics in the spatial domain [2]. We extended the simulation techniques used in our reference into the spectral domain by generating slices of single band images each with their own narrow response function to simulate the detectors. We generated images consistent with ones that would be collected by an adaptive spectral imaging system, but with wavelength centers that were similar to the HYDICE sensor.

We used an existing scene of Trona, CA, USA, that was routinely used for studies involving spectral images. Fig. 8 shows an image of this scene generated as a desert/industrial area where the background was attributed with spectra shown in Fig. 6. Fig. 9 shows an image of the same location, but generated as a suburban area where the background was attributed with the spectra shown in Fig. 5. This figure also shows how the entire scene was divided into subsets that produced nine different V_{scene} values. A subset scene that was more homogeneous such as subset nine, had lower V_{scene} values than the

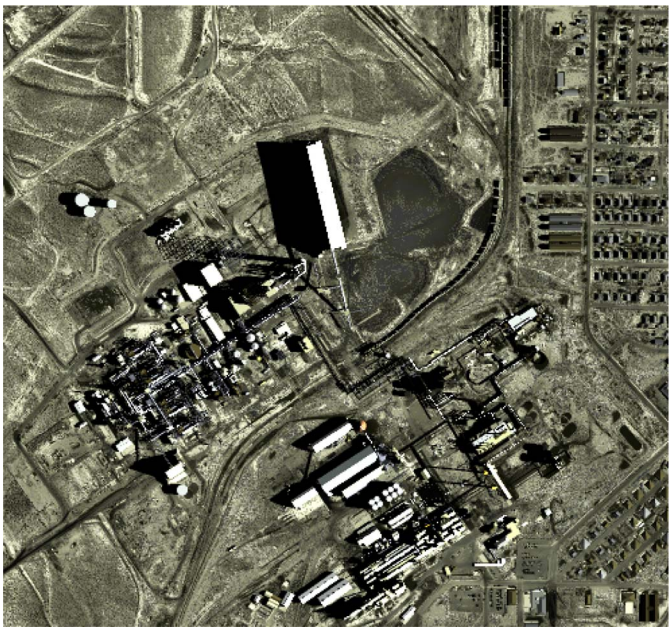

Fig. 8. High spatial resolution image of Trona, CA, USA, rendered as a desert scene.

Fig. 9. High spatial resolution image of Trona, CA, USA, rendered as suburban scene divided into nine subset scenes.

subsets with various structures and was heterogeneous such as subset seven.

Four types of vehicles were placed within the road network using the simulation of urban mobility (SUMO) [36], [37] where the location of the vehicles changed at time increments similar to real vehicles moving in traffic. When simulating multiple captures at a given rate, the location of the vehicles in each image was different from one image to another [38], [39]. This allowed a single simulation run to generate multiple images with changing target locations that were time correlated. This automated the workflow to generate 27 000 unique images using a few simulation designs, which ensured there was a sufficiently large sample set to draw statistically significant conclusions in the assessment process.

Fig. 10. Panels and array of vehicles used in scene attributed with each target material type.

Fig. 10 shows four calibration panels attributed with the target materials, and an array of the vehicle types that were placed within the scene. The panels attributed with the black and white materials were used for atmospheric compensation using the empirical line method [40]. The 18-wheeler was selected as a vehicle that was large enough to generate full target pixels. The dump truck was large enough to produce up to 0.85 TA, and the SUV and sedan were vehicles that could produce up to 0.45 TA. Since we were not "tracking" the targets, they did not always produce their maximum possible TA. The target was often spatially divided between several pixels and so there were TA variations in each scene. However, the different vehicle types generated their own median TAs which produced a distribution of TA values due to target size, relative spatial location to the pixel pitch, and GSD. In this way, we replicated an operational component of subpixel target detection that was not fully captured by the analytic prediction model.

Fig. 11 shows a high spatial resolution demonstration of a subset scene with the vehicles placed using SUMO as described earlier. With the semirandom placement of vehicles, there was potential for no targets of a certain type to be present in an image, or more than one of the target type to be present. We placed nine white and orange vehicles, and 15 green and black vehicles in the large scene. This produced statistically expected values of one white and orange vehicle in the subset scene, and 1.7 green and black vehicles. The movement files to place the vehicles were selected at random for each simulation set, which also introduced variations in the number of targets present. The extra use of green and black vehicles was to increase the TA_{mean} distribution by increasing the probability of higher pixel fill fractions from the good placement of a vehicle close to the center of a pixel since the detectable TA saturation points for these materials were higher.

In total, we generated sets of spectral images of the two scene types with the grass and sand backgrounds, that were

Fig. 11. High spatial resolution subset scene to demonstrate the placement of vehicles.

separated into nine subsets, where the vehicles and movement file combinations of these sets were selected using different random generator seeds. Each set simulated time captures of the randomly selected vehicle and movement file combinations for 20 s, at a rate of 1 image captured per second. A single run, therefore generated 20 images of the vehicles moving across a scene (or standing still) at various speeds. The image generation process was automated to run each simulation in parallel using high-performance computing resources.

E. Postprocessing and Utility Assessment

Once the images were generated, we needed to select bands, add noise, and apply a point spread function. We wanted to ensure that the synthetic images whose initial output was noiseless with perfect edge response functions, had real image characteristics. While fully replicating all real-world phenomena that affected utility was beyond the scope of this project, we wanted at the very least, to account for the major components of the imaging chain. The first step in preparing the data for assessment was to select the bands, not only because this was a critical component of the envisioned operational process but as a dimension reduction step to decrease computation requirements. The generated images were divided into six groups (GSD and background), and each group was divided into nine sets (subset scenes) for analysis. The same bands and the critical number of bands found in the prediction process were also used for the assessment process.

To each of the images, we added shot noise and parameterized the SNR. We combined both fixed and statistical noise as a single value, and multiplied the simulated images with a random value $[g(p, q, r)]$ that had a Gaussian distribution, zero mean, and unit standard deviation. Then, we scaled this value by the desired SNR to calculate the noise

$$n(p, q, r) = g(p, q, r) \cdot f(p, q, r)_{\text{sim}}/\text{SNR}. \tag{11}$$

In this equation, $f(p, q, r)_{\text{sim}}$ is the pixel value of the simulated image at the spatial location of p and q for the band r. This noise value was then added to the simulated image to produce the image that would on average have the desired SNR value

$$f(p, q, r)_{\text{noisy}} = f(p, q, r)_{\text{sim}} + n(p, q, r). \tag{12}$$

The separation of the noise contributions from different sources such as dark noise, and their effects on utility is a potential area of study for the future. However, in order to match the predicted noise analysis, we focused on shot noise.

Once the bands were selected and the noise was added, we convolved the image with a point spread function [41], [42]. We applied a blurring kernel to the noisy image using a discrete Fourier transform that replicated the effects of an Airy disc from a circular aperture whose size was related to the pixel. The Airy disc radius was set to $0.5 \cdot \lambda/\lambda_c$ for the 15-m GSD images, $1.0 \cdot \lambda/\lambda_c$ for the 10-m GSD images, and $1.5 \cdot \lambda/\lambda_c$ for the 5-m GSD images. Here, λ is the center wavelength of each band, and λ_c is the selected wavelength representing the overall sensor spectral band range, which in order to coincide with our panchromatic study was set to 0.5 μm [2]. This essentially replicated the optical resolution limits seen from increasing the focal length while the aperture diameter remained constant [43] where the 5-m GSD images had and Airy disc radius that was 0.5 times the pixel size, and the 15-m GSD images 1.5 times the pixel size.

We assessed the final utility using the postprocessed images by calculating the ROC curves. For the subset scenes of each background type and GSD, V_{scene} and TA_{mean} were calculated. A histogram was generated for each target in each set to evaluate the TA distributions of the target present pixels and find TA_{mean}. By calculating V_{scene}, Utility_{ψ}, and TA_{mean} values, we were able to find points of comparison for the assessment to the prediction, thus forming our trade space analysis process.

V. Results

From the prediction and assessment of utility we obtained from the eight target and background combinations, we were able to find novel relationships between trade space parameters. We used these findings to form mission feasibility and design recommendations for miniature spectral imaging systems. In this section, we present the SSVs that were calculated from the target and backgrounds as part of the prediction process. Then, we present the predicted utility trade curves that informed the recommendations. Finally, we present the assessment results and compare them to the utility predictions.

A. Spectral Similarity Values

The average curves of the targets and background types were used to calculate the SSVs shown in Table IV. Since the magnitude of the reflectance was used to calculate the SSV, their relationship to the background was relative. The green and black targets had lower SSVs overall because their reflectance magnitude was lower while the orange and white

TABLE IV
SPECTRAL SIMILARITY VALUES

Background/Target	White	Orange	Black	Green
Sand	0.28	0.46	0.07	0.21
Grass	0.42	0.39	0.25	0.14

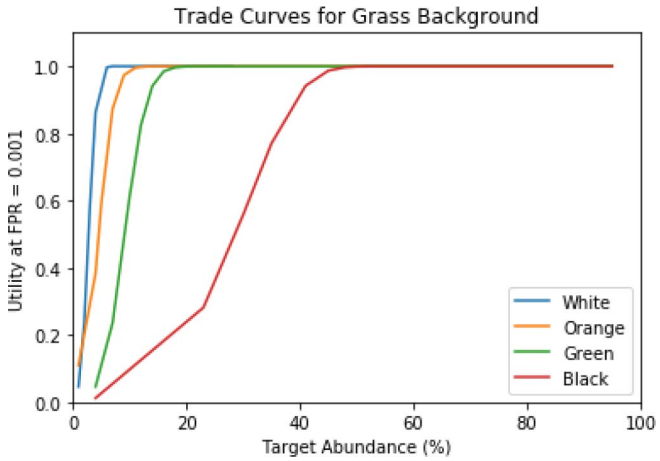

Fig. 12. Target abundance versus Utility$_\psi$ for grass background. *All* the bands were used to generate these results.

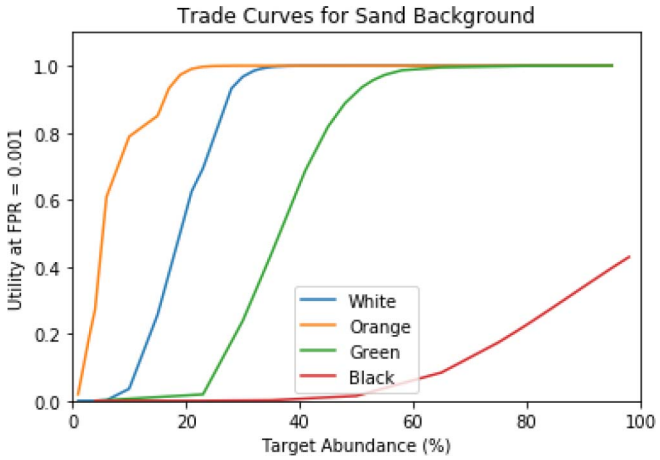

Fig. 13. Target abundance versus Utility$_\psi$ for sand background. *All* the bands were used to generate these results.

TABLE V
CRITICAL POINTS FOR TARGET ABUNDANCE

Background/Target	White	Orange	Black	Green
Sand	26%	18%	100%	58%
Grass	6%	11%	45%	16%

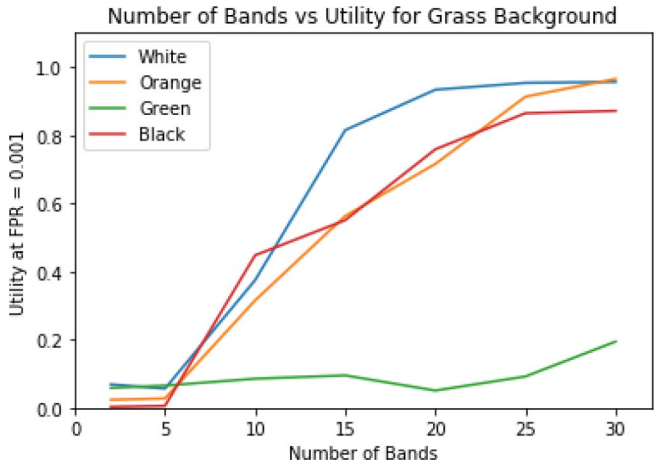

Fig. 14. Number of bands versus Utility$_\psi$ for grass background. The TA values in Table V were used to generate these curves.

target had higher SSVs. However, the green target relative to the black target had a lower SSV for the grass background than the sand background and vice versa for the black target, with similar relative relationships for the white and orange targets.

B. Prediction

The primary purpose of using an analytic model was to parameterize components that affected the trade space for subpixel target detection. We were able to generate trade curves for the four components efficiently without having to design hundreds of simulations. We analyzed the different dimensions within the spectral image utility trade space as separate slices and traversed through the space via the critical points.

1) Target Abundance: The eight detection scenarios were analyzed for the entire possible range of TA values. The critical point was the lowest TA value with Utility$_\psi$ > 0.98. We did not find a critical point for the black target in the sand background and Utility$_\psi$ < 0.4 even for full target pixels. Figs. 12 and 13 show the trade curves for the targets in the two background types. The brighter targets had critical points at relatively low TA values. The grass background was an easier background for subpixel target detection and a critical point was found for all the targets including the black target. Table V shows the critical points determined for the scenarios. These values were used to analyze Utility$_\psi$ versus the number of bands (L). The TA was fixed at the critical points to generate trade curves for the number of bands.

2) Number of Bands: We produced the trade curve for Utility$_\psi$ versus L using the top 30 bands selected using BOTS. The critical point for this parameter was set as the minimum L with Utility$_\psi$ > 0.9. Figs. 14 and 15 show the results of this analysis. For the easy targets, there was a clear point where L reach the critical point. The two difficult targets required more than 30 bands to produce Utility$_\psi$ > 0.9, and in Section V-B1, we saw that for the black target, even using all the bands did not produce this result.

Table VI shows the input values we used for the noise analysis. We set the maximum number of bands as $L = 30$ and used this and all the bands as input for the black and green targets. For the white and orange targets, we used the critical points found in this analysis. The low SSV between the target and background is a possible explanation for the seemingly inconsistent phenomena for the black and green target results. The green target in grass background resulted in Utility$_\psi$ > 0.98 when using all the bands, however, when reduced to 30 bands or less, the Utility$_\psi$ stagnated at 0.2. The black target on the other hand, Utility$_\psi$ continued to increase as the number of

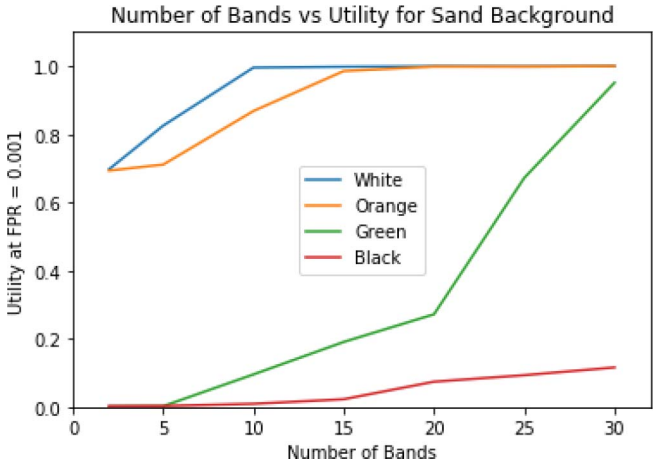

Fig. 15. Number of bands versus Utility$_\psi$ for sand background. The TA values in Table V were used to generate these curves.

TABLE VI
NUMBER OF BANDS USED FOR ANALYSIS INPUT

Background/Target	White	Orange	Black	Green
Sand	10	15	30	30
Grass	20	25	30	30

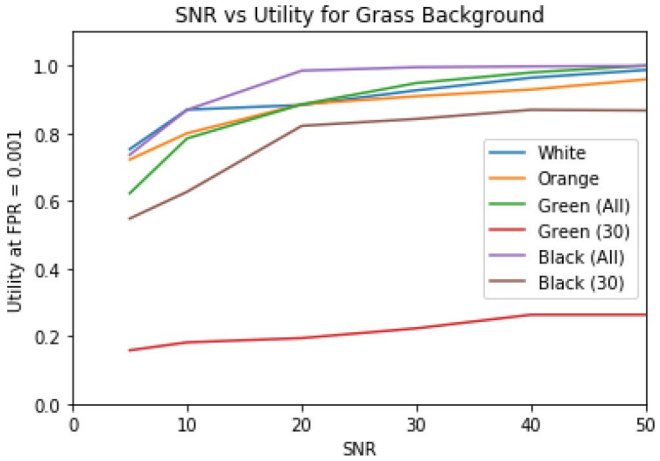

Fig. 16. Noise versus Utility$_\psi$ for grass.

bands did. Similar phenomena are seen for the green and black targets against the sand background but reversed.

3) Signal-to-Noise Ratio: We calculated Utility$_\psi$ for maximum SNR values of 5, 10, 20, 30, 40, and 50. Two separate studies were done for the green and black targets using 30 bands and all the bands. In general, while there was not a clear critical point for any of the scenarios, the trade curves reached a turning point at SNR $\geq$ 20 for all the scenarios. Therefore, this was the noise level that was added to the simulated images. Fig. 16 shows the trade curves for noise for the grass background. The sand background results were congruent to the grass background results for the evaluated range of SNR values. This analysis answered the question of whether or not the cost of improving the SNR was justified, and showed that it was not.

4) Background Complexity: The background surrounding a target greatly affects its detectability, and we parameterized the

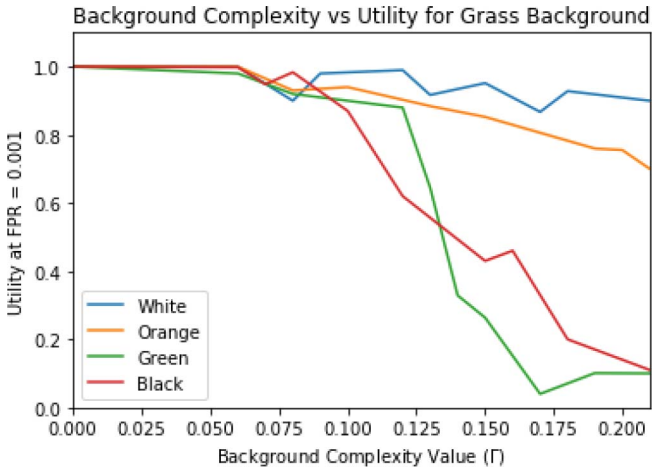

Fig. 17. Background complexity versus Utility$_\psi$ for grass.

background complexity by varying its composition within the model. Fig. 17 shows the predicted utility for a range of Γ values for the grass background. There is a clear trend where the utility decreases as the Γ value increases. The darker targets are affected more than the brighter targets. The sand background results were congruent to the grass background results for Γ, although the range of possible Γ values found was wider given the differences in reflectance between the materials and higher measurement variations used to compose this background.

C. Assessment

With the simulated images, we replicated the operational conditions for collection to validate the predictions. We designed a realistic scene to generate images that encompassed the critical points. In the assessment process, we combined the effects of target abundance and scene complexity to assess Utility$_\psi$. Images were generated at 5, 10, and 15 m GSDs. This produced TA distributions that were produced by the combined effects of the target size, the relative spatial position of the target to the pixel, and GSD. We introduced a detectability value that used the relationship between the TA_{mean} and V_{scene} of the sets. We produced a detectability versus Utility$_\psi$ curve for each GSD and background type to draw conclusions about the relationships between the imaging system parameters and the mission. These results combined with the predictions were used to form the mission feasibility and system design recommendations.

Fig. 18 shows a TA histogram of the positive pixels in set 5 of the desert scene that was rendered at 15-m GSD. The largest bins in the histogram are pixels below 0.01 TA. Fig. 19 shows the ROC curves generated from this set. The data were divided into 15-folds where a portion of the target present pixels and background pixels were randomly selected per fold. The detection statistics were calculated for each fold, and the colored lines are their ROC curves. The bold blue line in Fig. 19 is the mean ROC curve generated from the folds, and the gray area is the standard deviation.

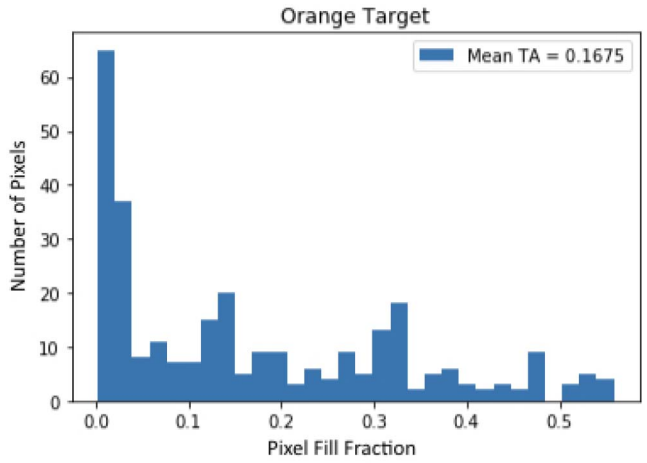

Fig. 18. Histogram of target fill fractions for the orange vehicles placed in the desert scene, set 5, rendered at 15-m GSD.

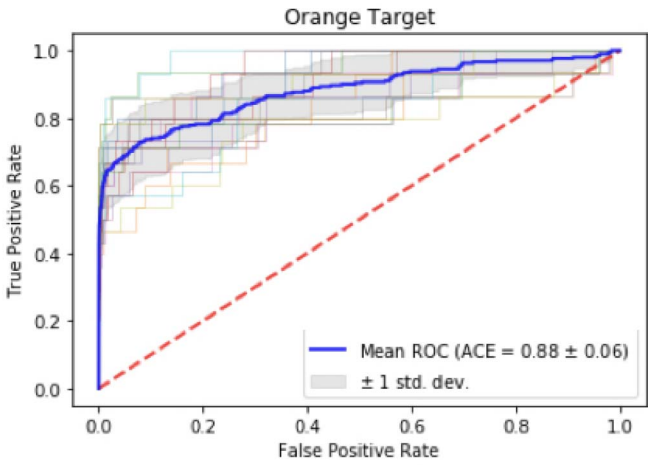

Fig. 19. ROC curve for orange vehicles in the desert scene, set 5, rendered at 15-m GSD. The gray area shows the standard deviation of ROC curves.

Each set rendered at the three different GSDs were first examined by their TA histograms, ROC curves, V_{scene}, and Utility$_\psi$. The complexity decreased and became similar between subset scenes as the GSD increased. The sets that had both open grass and residential buildings, such as set three and set seven, which when examined empirically had higher scene complexity, also had higher scene volumes. We use these values in our assessment of the imaging system design to calculate a detectability value (ξ). We calculated ξ by calculating the ratio between the TA_{mean} and V_{scene} for each set

$$\xi = \frac{TA_{mean}}{V_{scene}}. \tag{13}$$

A low TA_{mean} and high V_{scene} indicated a difficult detection scenario and so had low detectability. In our prediction, we determined that an imaging system whose mission was to find vehicles with the four material spectra should have optics that were capable of producing the TA critical points of each scenario. Thus, the three GSDs along with the vehicle sizes were selected to produce these TA values. We combined V_{scene} and TA_{mean} to introduce a metric that could be used to determine mission feasibility and system design recommendations.

TABLE VII
SCENE VOLUMES FOR DESERT BACKGROUND SIMULATION SETS

Set/Scene	5m GSD	10m GSD	15m GSD
1	0.47	0.70	0.41
2	0.64	0.31	0.40
3	0.46	0.40	0.30
4	0.30	0.47	0.39
5	0.44	0.41	0.41
6	0.40	0.37	0.42
7	0.32	0.43	0.43
8	0.38	0.49	0.45
9	0.49	0.87	0.44

TABLE VIII
SCENE VOLUMES FOR SUBURB BACKGROUND SIMULATION SETS

Set/Scene	5m GSD	10m GSD	15m GSD
1	0.50	0.48	0.41
2	0.61	0.45	0.40
3	0.62	0.40	0.30
4	0.47	0.59	0.38
5	0.58	0.56	0.39
6	0.44	0.41	0.40
7	0.82	0.50	0.42
8	0.61	0.46	0.45
9	0.63	0.55	0.44

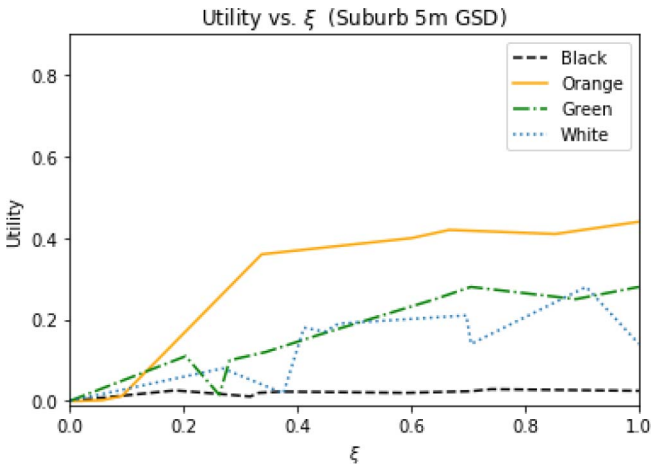

Fig. 20. Utility$_\psi$ for each ξ value, calculated for the suburban scene, rendered at 5-m GSD.

For each background and GSD, we calculated ξ, sorted these values, then plotted the Utility$_\psi$ calculated for the sets. Tables VII and VIII show the scene volumes that were calculated for each scene set.

Figs. 20 and 21 show the ξ versus Utility$_\psi$ curves of the 5- and 15-m GSD desert scenes. The curves show that the orange, green, and white targets had increasing Utility$_\psi$ as ξ increased, while the black target, had Utility$_\psi$ < 0.1 independent of ξ.

D. Example Requirement Recommendation Flow Diagram

In this section, we present an example set of recommendations formed using this process for two potential missions. The trade curves were used to drive the final system parameter recommendations and the mission feasibility determination.

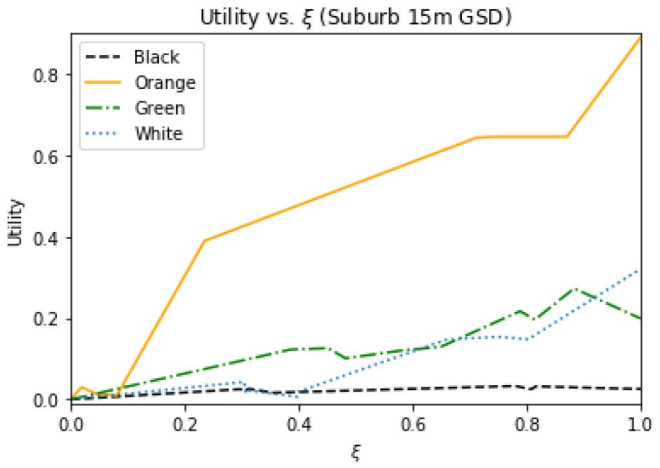

Fig. 21. Utility$_\psi$ for each ξ value, calculated for the suburban scene, rendered at 15-m GSD.

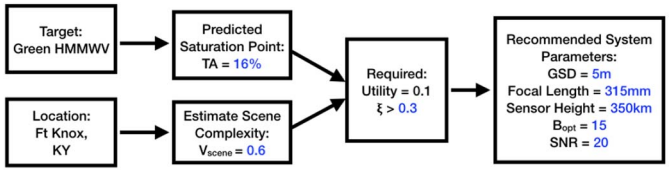

Fig. 22. Example use of process leading to imaging system parameter recommendation for a green target with using the scene volume metric. Required Utility$_\psi$ for this mission is 0.1, leading to recommended parameters that result in $\xi > 0.3$.

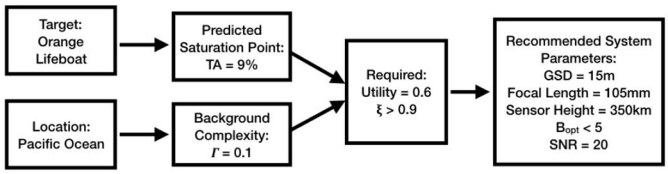

Fig. 23. Example use of process leading to imaging system parameter recommendation for orange target using background complexity metric.

TABLE IX
LIST OF ACRONYMS

ACE	Adaptive Cosine Estimator
AUC	Area Under the Curve
BOTS	Bands from Only the Target Spectrum
CEM	Constrained Energy Minimzer
DIRSIG	Digital Imaging and Remote Sensing Image Generation
FASSP	Forecasting and Analysis of Spectro-radiometric System Performance
FPR	False Positive Rate
GIQE	General Image Quality Equation
GSD	Ground Sampled Distance
HSI	Hyperspectral Images
HYDICE	Hyperspectral Digital Imagery Collection Experiment
MODTRAN	Moderate Resolution Transmission
ROC	Receiver Operating Characteristic
SAM	Spectral Angle Mapper
SMF	Spectral Matched Filter
SNR	Signal-to-Noise Ratio
SSV	Spectral Similarity Value
SUMO	Simulation of Urban Mobility
TA	Target Abundance or Target Fill Fraction
TPR	True Positive Rate
VNIR	Visible Near Infrared

Fig. 22 shows a flow diagram for a challenging mission with low Utility$_\psi$ requirement but determined as feasible. This mission was feasible because other assets were readily available to confirm or deny the presence of a target. We used the predicted TA saturation point, and the estimated V_{scene} for the location. The example location we used was Fort Knox, KY, USA, which resembled the subset scenes 2 and 8 of the suburban scene. For the green target in a location consisting mostly of vegetation, Utility$_\psi > 0.1$ if $\xi > 0.3$. We compared the results shown in Figs. 20 and 21 and found that the 5-m GSD had better results for the green target. Therefore, the focal length and sensor height that produce this GSD were the recommended system parameters. From Fig. 14, Utility$_\psi > 0.1$ with 15 bands, and so this was the recommended L. We determined that this mission was feasible if the operation only required Utility$_\psi < 0.3$ as this was the maximum Utility$_\psi$ only achievable if $\xi > 0.7$.

Fig. 23 shows another example of a target detection mission that used the Γ instead of V_{scene}. The curves for the orange target in Figs. 20 and 21 show better performance for the scene rendered at 15-m GSD. This background however was an open ocean scene that did not have any inherent structures that contributed to the complexity. It is why Γ was an appropriate metric since the scene was homogeneous, and because of this the expected ξ value was greater than 0.9. For the location and type of target, this mission was appropriate for a wider range of operational conditions and feasible even if the required Utility$_\psi$ was higher. A possible situation would be if the constellation of miniature satellites was the only asset available for target detection with limited ability for confirmation of target presence. A higher Utility$_\psi$ would be required, implying a need for smaller FPR in this situation.

VI. Conclusion and Future Work

In designing a compact spaceborne imaging system with the mission scenario as the input, we analyzed target abundance and scene complexity to provide system design recommendations for GSD, SNR, and the number of bands. In this article, we presented novel system metrics together with a process that used them to find the relationships within the spectral utility trade space for miniature spaceborne systems. We coupled the mission scenario and operational requirements to the design components of spectral imaging systems. Improving spatial resolution increased the distribution mean of the TA which could improve the utility, but it also increased scene complexity which decreased utility. The trade decisions for determining system parameters were based on the target, background, and operational requirements.

Some other areas of study for the future are the use of this process for other mission scenarios and targets. We can explore the trade between GSD and the number of bands, and the effects of changing the coefficients used to select the bands in the future. We can also consider the effects of larger scenes and context for utility as the total scene size increases even as the spatial resolution decreases. In this article, we presented a process that used existing modeling tools in a novel manner to comprehensively analyze the spectral utility

trade space for both the design and operation processes. The relationships between each component were complex, but we found key trends in the relationship between the system parameters to form mission feasibility and design recommendations. Characterization of these relationships with further analysis is another direction for future work.

REFERENCES

[1] V. Riot, "Space program innovation, one small satellite at a time," *Sci. Technol. Rev.*, pp. 4–11, Apr. 2019.

[2] S. Han, S. Higbee, L. Siegel, and J. P. Kerekes, "Simulation techniques for image utility analysis," in *Proc. SPIE Conf.*, May 2018, p. 25.

[3] J. C. Leachtenauer, W. Malila, J. Irvine, L. Colburn, and N. Salvaggio, "General image-quality equation: GIQE," *Appl. Opt.*, vol. 36, no. 32, p. 8322, Nov. 1997.

[4] S. S. Shen, "Spectral quality equation relating collection parameters to object/anomaly detection performance," in *Proc. SPIE Conf. AeroSense*, Sep. 2003, p. 29.

[5] J. P. Kerekes and S. M. Hsu, "Spectral quality metrics for VNIR and SWIR hyperspectral imagery," in *Proc. SPIE Conf. Defense Security*, Aug. 2004, p. 549.

[6] J. P. Kerekes, A. P. Cisz, and R. E. Simmons, "A comparative evaluation of spectral quality metrics for hyperspectral imagery," in *Proc. SPIE Conf. Defense Security*, Jun. 2005, p. 469.

[7] R. E. Simmons *et al.*, "General spectral utility metric for spectral imagery," in *Proc. SPIE Conf. Defense Security*, Jun. 2005, p. 457.

[8] M. Stefanou and J. Kerekes, "A method for assessing spectral image utility," *IEEE Trans. Geosci. Remote Sens.*, vol. 47, no. 6, pp. 1698–1706, Jun. 2009.

[9] J. Kerekes and D. Landgrebe, "Simulation of optical remote sensing systems," *IEEE Trans. Geosci. Remote Sens.*, vol. 27, no. 6, pp. 762–771, Nov. 1989.

[10] J. P. Kerekes and D. A. Landgrebe, "An analytical model of Earth-observational remote sensing systems," *IEEE Trans. Syst., Man, Cybern., Syst.*, vol. 21, no. 1, pp. 125–133, Feb. 1991.

[11] J. Kerekes and D. Landgrebe, "Parameter trade offs for imaging spectroscopy systems," *IEEE Trans. Geosci. Remote Sens.*, vol. 29, no. 1, pp. 57–65, Jan. 1991.

[12] X. Cao, F. Zhang, X. Lin, Z. Sun, and G. Xu, "Optical remote sensing small satellite project," *Acta Astronautica*, vol. 54, no. 2, pp. 139–143, Jan. 2004.

[13] A. Jafarsalehi, H. Fazeley, and M. Mirshams, "Conceptual remote sensing satellite design optimization under uncertainty," *Aerosp. Sci. Technol.*, vol. 55, pp. 377–391, Aug. 2016.

[14] N. Li, P. Huang, H. Zhao, and G. Jia, "The quantitative evaluation of application of hyperspectral data based on multi-parameters joint optimization," *Sci. China Technol. Sci.*, vol. 57, no. 11, pp. 2249–2255, Nov. 2014.

[15] D. Kaslow, G. Soremekun, H. Kim, and S. Spangelo, "Integrated model-based systems engineering (MBSE) applied to the Simulation of a CubeSat mission," in *Proc. IEEE Aerosp. Conf.*, Mar. 2014, pp. 1–14. [Online]. Available: http://ieeexplore.ieee.org/document/6836317/

[16] R. Duca and F. Del Frate, "Hyperspectral and multiangle CHRIS-PROBA images for the generation of land cover maps," *IEEE Trans. Geosci. Remote Sens.*, vol. 46, no. 10, pp. 2857–2866, Oct. 2008. [Online]. Available: http://ieeexplore.ieee.org/document/4637938/

[17] H. Jin, P. Li, T. Cheng, and B. Song, "Land cover classification using CHRIS/PROBA images and multi-temporal texture," *Int. J. Remote Sens.*, vol. 33, no. 1, pp. 101–119, Jan. 2012. [Online]. Available: https://www.tandfonline.com/doi/full/10.1080/01431161.2011.584077

[18] J. Delegido, G. Fernández, S. Gandía, and J. Moreno, "Retrieval of chlorophyll content and LAI of crops using hyperspectral techniques: Application to PROBA/CHRIS data," *Int. J. Remote Sens.*, vol. 29, no. 24, pp. 7107–7127, Dec. 2008. [Online]. Available: https://www.tandfonline.com/doi/full/10.1080/01431160802238401

[19] M. Esposito, S. S. Conticello, M. Pastena, and B. C. Dománguez, "In-orbit demonstration of artificial intelligence applied to hyperspectral and thermal sensing from space," in *Proc. CubeSats SmallSats Remote Sens.*, vol. 11131, 2019, pp. 88–96. [Online]. Available: https://doi.org/10.1117/12.2532262

[20] M. S. Stefanou, "Spectral image utility for target detection applications," Ph.D. dissertation, Center Imag. Sci., Rochester Inst. Technol., Rochester, NY, USA, Aug. 2008. [Online]. Available: https://scholarworks.rit.edu/theses/2910/

[21] O. A. Weaver, "An analytical framework for assessing efficacy of small satellites in performing imaging missions," Ph.D. dissertation, Center Imag. Sci., Rochester Inst. Technol., Rochester, NY, USA, Jul. 2015. [Online]. Available: https://scholarworks.rit.edu/theses/8766/

[22] S. Han, J. Kerekes, S. Higbee, L. Siegel, and A. Pertica, "Band selection method for subpixel target detection using only the target signature," *Appl. Opt.*, vol. 58, no. 11, p. 14, 2019.

[23] J. N. Sweet, M. H. Sharp, and J. C. Granahan, "Hyperspectral analysis toolset," in *Proc. SPIE Conf. Europe Remote Sens.*, Feb. 2001, pp. 396–407. [Online]. Available: http://proceedings.spiedigitallibrary.org/proceeding.aspx?articleid=923961

[24] M. T. Eismann, *Hyperspectral Remote Sensing*. Bellingham, WA, USA: SPIE Press, 2012.

[25] D. W. Messinger, A. Ziemann, B. Baesner, and A. Schlamm, "Metrics of spectral image complexity with application to large area search," *Opt. Eng.*, vol. 51, no. 3, Mar. 2012, Art. no. 036201.

[26] F. Kruse, A. Lefkoff, and J. Dietz, "Expert system-based mineral mapping in northern death valley, California/Nevada, using the airborne visible/infrared imaging spectrometer (AVIRIS)," *Remote Sens. Environ.*, vol. 44, no. 2, pp. 309–336, 1993.

[27] D. Manolakis and G. Shaw, "Detection algorithms for hyperspectral imaging applications," *IEEE Signal Process. Mag.*, vol. 19, no. 1, pp. 29–43, Jan. 2002.

[28] L. L. Scharf and B. Friedlander, "Matched subspace detectors," *IEEE Trans. Signal Process.*, vol. 42, no. 8, pp. 2146–2157, Aug. 1994.

[29] C.-I. Chang, "Generalized constrained energy minimization approach to subpixel target detection for multispectral imagery," *Opt. Eng.*, vol. 39, no. 5, pp. 1275–1281, May 2000.

[30] J. Kerekes and J. Baum, "Spectral imaging system analytical model for subpixel object detection," *IEEE Trans. Geosci. Remote Sens.*, vol. 40, no. 5, pp. 1088–1101, May 2002.

[31] A. Berk *et al.*, "MODTRAN cloud and multiple scattering upgrades with application to AVIRIS," *Remote Sens. Environ.*, vol. 65, no. 3, pp. 367–375, Sep. 1998.

[32] J. Kerekes, "Model-based exploration of HSI spaceborne sensor requirements with application performance as the metric," in *Proc. IEEE Int. Symp. Geosci. Remote Sens.*. Jul. 2006, pp. 1613–1616.

[33] A. A. Goodenough and S. D. Brown, "DIRSIG5: Next-generation remote sensing data and image simulation framework," *IEEE J. Sel. Topics Appl. Earth Observ. Remote Sens.*, vol. 10, no. 11, pp. 4818–4833, Nov. 2017.

[34] S. Han, "Utility analysis for optimizing compact adaptive spectral imaging systems for subpixel target detection applications," Center Imag. Sci., Rochester Inst. Technol., Rochester, NY, USA, Jul. 2019. [Online]. Available: https://scholarworks.rit.edu/theses/10247/

[35] L. J. Rickard, R. W. Basedow, E. F. Zalewski, P. R. Silverglate, and M. Landers, "HYDICE: An airborne system for hyperspectral imaging," in *Proc. Opt. Eng. Photon. Aerosp. Sens.*, Sep. 1993, p. 173.

[36] P. A. Lopez *et al.*, "Microscopic traffic simulation using SUMO," in *Proc. IEEE 21st Int. Conf. Intell. Transport. Syst. (ITSC)*, Nov. 2018, pp. 2575–2582.

[37] R. Hilbrich. *SUMO—Simulation of Urban MObility DLR—Institute of Transporation*. [Online]. Available: https://sumo.dlr.de/wiki/Simulation_of_Urban_MObility_-_Wiki

[38] M. D. Presnar, A. D. Raisanen, D. R. Pogorzala, J. P. Kerekes, and A. C. Rice, "Dynamic scene generation, multimodal sensor design, and target tracking demonstration for hyperspectral/polarimetric performance-driven sensing," in *Proc. SPIE Conf. Defense Security Sens.*, Orlando, FL, USA, Apr. 2010, Art. no. 76720T.

[39] S. Han *et al.*, "Efficient generation of image chips for training deep learning networks," in *Proc. SPIE Conf. Defense Security*, vol. 10202. Anaheim, CA, USA, May 2017, Art. no. 1020203.

[40] J. D. Ortiz *et al.*, "Intercomparison of approaches to the empirical line method for vicarious hyperspectral reflectance calibration," *Front. Marine Sci.*, vol. 4, p. 296, Sep. 2017. [Online]. Available: http://journal.frontiersin.org/article/10.3389/fmars.2017.00296/full

[41] T. P. Robitaille, and E. J. Tollerud, "Astropy: A community Python package for astronomy," *Astronomy Astrophys.*, vol. 558, p. A33, Oct. 2013.

[42] A. M. Price-Whelan and A. Donath, "The astropy project: Building an open-science project and status of the v2.0 core package," *Astron. J.*, vol. 156, no. 3, p. 123, Aug. 2018.

[43] R. D. Fiete, "Image quality and λFN/p for remote sensing systems," *Opt. Eng.*, vol. 38, no. 7, p. 1229, Jul. 1999.

Sanghui Han (Student Member, IEEE) received the B.S. degree in applied mathematics from the University of Colorado, Colorado Springs, CO, USA, in 2007, and the M.S. degree in imaging science from the Rochester Institute of Technology, Rochester, NY, USA, in 2015, where she is currently pursuing the Ph.D. degree in imaging science.

From 2000 to 2015, she served in the United States Army first as an enlisted Soldier in the medical field. Then she was commissioned as a CBRNE Officer where she specialized in WMD operations and training and then as an Intelligence Officer where she specialized in signals intelligence, collection, and analysis. Her current research topics involve spectral image utility assessment and prediction for sensor design using image simulation and modeling.

Dr. Han is a Student Member of the Optical Society of America and SPIE.

John Kerekes (Senior Member, IEEE) received the B.S., M.S., and Ph.D. degrees in electrical engineering from Purdue University, West Lafayette, IN, USA, in 1983, 1986, and 1989, respectively.

From 1983 to 1984, he was a Technical Staff Member with the Space and Communications Group, Hughes Aircraft Company, El Segundo, CA, USA, where he performed circuit design for communications satellites. From 1986 to 1989, he was a Graduate Research Assistant with the School of Electrical Engineering and the Laboratory for Applications of Remote Sensing, Purdue University. From 1989 to 2004, he was a Technical Staff Member with the Lincoln Laboratory, Massachusetts Institute of Technology, Lexington, MA, USA. Since 2004, he has been with the Chester F. Carlson Center for Imaging Science, Rochester Institute of Technology, Rochester, NY, USA, where he is currently a Professor. His research interests include the modeling and analysis of remote sensing system performance in pattern recognition and geophysical parameter retrieval applications.

Prof. Kerekes served as the Founding Chair of the Boston Section Chapter of the IEEE Geoscience and Remote Sensing Society (GRSS) from 1995 to 2004 and the Western New York Chapter of GRSS from 2007 to 2010. He was the Co-General Chair of the IEEE International Geoscience and Remote Sensing Symposium in 2008 held in Boston, MA, USA. He is a member of Tau Beta Pi, Eta Kappa Nu, the American Geophysical Union, and the American Society for Photogrammetry and Remote Sensing. From 2010 to 2015, he was a member of the GRSS Administrative Committee, including service as the Vice President of Technical Activities from 2011 to 2015. In January 2017, he was appointed Chief Financial Officer of the GRSS. He is a Senior Member of the Optical Society of America and SPIE.

Shawn Higbee, photograph and biography not available at the time of publication.

Lawrence Siegel, photograph and biography not available at the time of publication.